11-1-2022

Optimizing Switching of Non-linear Properties with Hyperbolic Metamaterials

James A. Ethridge
Air Force Institute of Technology

John G. Jones
Air Force Research Laboratory

Manuel R. Ferdinandus
Air Force Institute of Technology

Michael J. Havrilla
Air Force Institute of Technology

Michael A. Marciniak
Air Force Institute of Technology

Recommended Citation

James A. Ethridge, John G. Jones, Manuel R. Ferdinandus, Michael J. Havrilla, and Michael A. Marciniak, "Optimizing switching of non-linear properties with hyperbolic metamaterials," Opt. Mater. Express 12, 4471-4483 (2022).https://doi.org/10.1364/OME.471570

Research Article | Vol. 12, No. 11 / 1 Nov 2022 / Optical Materials Express 4471
Optical Materials EXPRESS

Optimizing switching of non-linear properties with hyperbolic metamaterials

JAMES A. ETHRIDGE,[1,*] JOHN G. JONES,[2] MANUEL R. FERDINANDUS,[3] MICHAEL J. HAVRILLA,[1] AND MICHAEL A. MARCINIAK[1]

[1]Air Force Institute of Technology, 2950 Hobson Way, WPAFB, OH 45433, USA
[2]Air Force Research Laboratory, Materials and Manufacturing Directorate, 2941 Hobson Way, WPAFB, OH 45433, USA
[3]Centauri, 15020 Conference Center Drive STE 100, Chantilly, VA 20151, USA
[*]james.ethridge.7@us.af.mil

Abstract: Hyperbolic metamaterials have been demonstrated to have special potential in their linear response, but the extent of their non-linear response has not been extensively modeled or measured. In this work, novel non-linear behavior of an ITO/SiO_2 layered hyperbolic metamaterial is modeled and experimentally confirmed, specifically a change in the sign of the non-linear absorption with intensity. This behavior is tunable and can be achieved with a simple one-dimensional layered design. Fabrication was performed with physical vapor deposition, and measurements were conducted using the Z-scan technique. Potential applications include tunable optical switches, optical limiters, and tunable components of laser sources.

1. Introduction

Hyperbolic metamaterials (HMMs) are materials which exhibit hyperbolic isofrequency surfaces, which occur when a uniaxial material has the property that $\epsilon_{xx}, \epsilon_{yy}>0$ and $\epsilon_{zz}<0$ or $\epsilon_{xx}, \epsilon_{yy}<0$ and $\epsilon_{zz}>0$. For HMMs, there is a transition point from standard behavior, which is described by an elliptical isofrequency surface, to hyperbolic behavior. This transition occurs at the epsilon-near-zero (ENZ) point, since changing from positive to negative permittivity or vice versa requires crossing the zero point. There are several different ways to achieve hyperbolic behavior, including nanowires and multi-layer metal-dielectric stacks [1–3]. This work uses the multi-layer metal-dielectric stacks, which have well-known linear properties that can be represented by an effective medium approximation (EMA). This formulation applies when the layer thicknesses are much smaller than the wavelength of interest, which is the case in this work. Equation (1) shows the Maxwell-Garnett EMA for ϵ_{xx} or ϵ_{yy}:

$$\epsilon_{xx,yy} = \rho\epsilon_m + (1-\rho)\epsilon_d, \tag{1}$$

where ρ is the metal fraction, ϵ_m is the permittivity of the metal layer, and ϵ_d is the permittivity of dielectric layer. The equation for ϵ_{zz} is also well known [2], thus it does not need to be shown here. Using this formulation, it is possible to calculate the linear properties of a HMM such as the ENZ point. The optical properties at ENZ point, the special density of states, and other properties of HMMs have led to many promising developments for applications such as waveguides [4], thermal control [5,6], and various quantum applications [7,8]. In addition, HMMs in general can have non-linear behavior and applications, such as frequency conversion [9], optical switching [10–14], and emission control [15,16]. The optical switching application of HMMs is chosen as a focus in this work. Most work on this topic to this point has been single point designs [17] or purely theoretical methods [11].

The focus of this work is on non-linear properties, which are properties of materials that are proportional to the field in some way, depending on their order. The multi-layer HMMs are

#471570 https://doi.org/10.1364/OME.471570
Journal © 2022 Received 16 Aug 2022; revised 7 Sep 2022; accepted 10 Sep 2022; published 27 Oct 2022

Optical Materials EXPRESS

centrosymmetric, thus by definition, their second order properties become zero [18]. Therefore third order properties are used in this work, which are proportional to the square of the electric field. Since the square of the electric field is proportional to the intensity, it can be said that the third order non-linear proprieties are proportional to intensity. Equations (2) and (3) show the effective refractive index and absorption including these third order non-linear effects:

$$n = n_0 + n_{2_{\text{eff}}} I, \tag{2}$$

$$\alpha = \alpha_0 + \beta_{\text{eff}} I, \tag{3}$$

where I is the input intensity. Calculating the linear properties (n_0, α_0) and non-linear properties (n_2, β) would allow for full characterization of the material. With an intensity dependent effective refractive index or absorption coefficient, it is possible to achieve a sample where transmission will change with intensity. This property then allows for all-optical switching, since when this material is placed in a cavity that is tuned correctly, switching between two or more transmission states can be achieved. This optical switching has many applications, with one major application being optical computing, as a component of optical memory [19,20].

For most non-linear materials that have been studied, when considering non-linear absorption, the transmission will monotonically increase or decrease with intensity [18]. However, the materials studied in this work actually switch from decreasing with intensity to increasing with intensity due to their HMM properties. To investigate this, this work uses a optimization routine that investigates many parts of the design space, then the optimized designs are verified with experiment. The behavior where the sign of the non-linear absorption coefficient changes with intensity is modeled and verified; this has the ability to increase the all-optical switching potential of HMMs by giving access to more transmission states and easily tunable behavior.

The fabrication and modeling methods are presented first, followed by the the optimization results and measurements, and lastly, an uncertainty analysis with comparisons of the model to the measurement is performed.

2. Methodology

2.1. Fabrication

The basic design of the metamaterials is comprised of alternating layers of metal and dielectric, on either a glass or silicon substrate depending on the intended application. The materials used were indium tin oxide (ITO) as the metal and silica (SiO_2) as the dielectric. Since the wavelengths of interest are in the near infrared, ITO behaves like a standard Drude metal for its linear properties [21].

The fabrication process of the HMMs is physical vapor deposition, accomplished through magnetron sputtering. Magnetron sputtering uses uses a cascade process of ionization of inert gas such as Ar and a magnet to increase ion density and energy at the surface of the target material, causing ejection of material from the ionized bombardment that will deposit the target source material onto the substrate. The advantages of sputtering are that it works more easily on high melting point and conducting materials where other methods are difficult, and adheres better than other methods [22,23].

The power supply can also accept a setting of "reverse time" in microseconds which is used to "discharge" the target material. For the SiO_2 reactive sputtering, a Si target was used with oxygen present in deposition chamber. This oxygen could remain the same throughout the deposition, since the ITO layer was not impacted by the presence of oxygen. For the SiO_2 sputtering, the 120 W power setting was used, with 80 kHz pulse rate and 4.5 μs reverse time; which results in pulsed DC magnetron sputter. The sputtering process could also be operated in a constant 120 W mode, which would be DC magnetron sputtering, but with SiO_2 and reactive sputtering, the Si target material would have oxidized and an excessively high voltage would have been

Optical Materials EXPRESS

required by the power supply causing the system to shut off. The reverse voltage prevents this process by discharging the target, preventing significant charge build up, allowing sputtering to continue. The ITO deposition used DC magnetron sputtering at 60 W. For initial test samples, depositions were done at room temperature, but for the samples in this work, the temperature of the substrate was heated to 400 degrees Celsius for the deposition of the ITO layers. This improved the consistency of fabrication of the samples.

To verify that fabrication was successful, transmission electron microscope (TEM) images of some of the samples were taken. Figure 1 shows a representative TEM image. From the figure, it can be seen that the layer deposition was successful, though there is some level of interface roughness that increases as more layers are deposited. Using image analysis software on the images with an included length scale, the standard deviation in layer thickness was calculated to be about 2.35 nm, though this number is not exact due to the layers not being perfectly flat. Since a 28.95% metal fraction was the design goal, this implies that the true metal fraction falls between 27.7% and 30.2% for one standard deviation and 26.5% and 31.4% for two standard deviations.

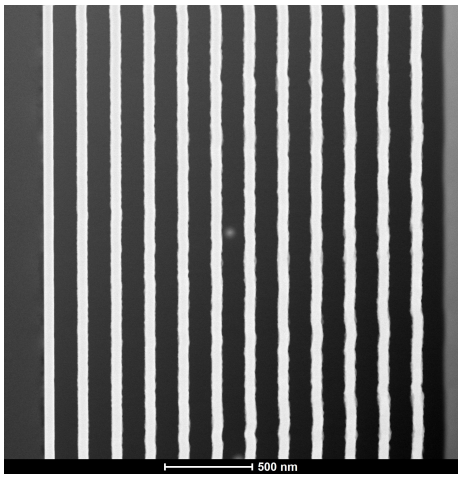

Fig. 1. TEM images of a Representative HMM Sample. The brighter layers are the ITO layers, and the darker layers are the SiO_2. Note that the design for this image was 55 nm of ITO and 135 nm SiO_2 for a repetition of 12 periods, or 24 total layers on a silicon substrate. Later it will be shown that this geometry is in the range of optimal designs.

2.2. Modeling

Modeling the non-linear switching properties of HMMs has been done in different ways in the literature [10,11,13,14], but to our knowledge, there has not been genetic algorithm optimization of the designs performed. Therefore, leveraging modeling schemes that have already been verified, this work will use the genetic algorithm to optimize for a non-linear application, specifically switching, and verify the results. Matching the modeling results with experiment is also a key feature of this work, as the other work cited above on switching properties of HMMs has been solely simulation based. There are many possible design geometries, and of course it is not possible to fabricate and measure hundreds of samples. Therefore computational schemes that can accurately account for changing design geometries are required.

The first task of the model involves calculation of non-linear properties of the metal layer, including the field enhancement effects that occur when the laser beam is incident at an oblique angle (for TM polarization). Equation (4) [21] defines the field enhancement, which follows from

Optical Materials EXPRESS

the field continuity at the interface between the air and material.

$$E^{\perp}_{\text{mat}} = \frac{E^{\perp}_{\text{air}}}{\epsilon_{\text{mat}}}, \tag{4}$$

where $E^{\perp}_{\text{mat}}$ is the electric field in the material oriented normal to the interface, $E^{\perp}_{air}$ is the incident electric field oriented normal to the interface, and ϵ_{mat} is the complex permittivity of the material. This implies that a smaller ϵ of the material gives greater field enhancement, which is generally the case near to the ENZ point. This permittivity can be found from the geometry and base material properties using Eq. (1). Also, since this applies to the normal components of the fields, this factor will be zero at zero degrees incident, but will generally increase as the obliqueness of the angle increases. There is a limiting factor, that of Fresnel reflections that increase when the incident angle increases, so the optimal angle is will be much lower than 90 degrees. The optimal angle is generally between 50 to 75 degrees, but this depends on the linear properties of the material. The linear reflection and transmission behavior is accounted for using a transfer matrix method in this work, which is a common method for multi-layer stacks [24].

To begin to account for non-linear properties, including this field enhancement, the two temperature model (TTM) is used. The TTM models the evolution of the electron temperature and lattice temperature, with the lattice temperature representing the properties of the phonons. The TTM can account for very large effective non-linear properties, assuming that the metal can be appropriately represented by a Drude model; this technique has been applied to various material systems [25]. This technique has been successfully applied to ITO films in [21], and this work uses that exact formulation. In this formulation, the elevated electron temperature is calculated directly from the TTM, for a specific wavelength, angle and intensity, which gives an elevated chemical potential (Fermi level). This elevated Fermi level leads to a change in the plasma frequency, which corresponds to Δn and a $\Delta\alpha$ using the Drude model. From these, it is possible to calculate n_2 and β since $n_{2_{\text{eff}}} = \frac{\Delta n}{I}$ and $\beta_{\text{eff}} = \frac{\Delta\alpha}{I}$. This gives non-linear properties of the ITO layer in the HMMs that are dependent on input wavelength, angle, and intensity.

Next, to convert HMM properties, a non-linear EMA can be applied that was specifically designed in [26] for materials with alternating metal and dielectric layers. This is the simple extension of the Maxwell-Garnett EMA discussed earlier to the non-linear properties. The formulation for TM polarization is shown in Eq. (5).

$$\chi^{(3)}_{\text{EMA}} = \rho\chi^{(3)}_{m} + (1-\rho)\chi^{(3)}_{d}, \tag{5}$$

where $\chi^{(3)}_{m}$ is the third-order susceptibility of the metal layer, $\chi^{(3)}_{d}$ is the third-order susceptibility of the dielectric layer, and ρ is the metal fraction, as before. The form of Eq. (5) can be seen to be the same as Eq. (1). The equation for TE polarization is not shown, as only TM polarization was used in this work. The third-order susceptibility of the metal layer can be found using the TTM as discussed above, since the complex third-order susceptibility, $\chi^{(3)}$, can be derived with the n_2 and β values from the TTM, in a similar fashion to $\chi^{(1)}$ being derived from n and k. However, using this equation also requires the third-order susceptibility of the dielectric layer. To account for this, values from the literature for SiO_2 were used [27], and they were confirmed with measurement.

These properties were placed into a full field simulation in the software *Lumerical*, and a genetic algorithm was used to find optimal designs, which is a technique that has been used previously [28]. The genetic algorithm lends itself well to optimization problems that are multi-objective and not clearly defined by a differentiable function, which is the case in this work. Other optimization algorithms could have been used, but the genetic algorithm was found to be the simplest to integrate into the model that had already been completed.

In general, the genetic algorithm works by mimicking natural evolution process, with a population that undergoes random changes ("mutation") and inheritance. The population

Optical Materials EXPRESS

members that perform the best on the chosen fitness functions are more likely to have their properties inherited to the next generation of the population. As the generations progress, this leads to better and better performing population members, and then at some cutoff point, normally a certain number of generations, the population member with best fitness function performance is called the optimal solution.

In this work, the desired fitness functions are the switching intensity and the switching width. The switching intensity is defined here as the input intensity where the sign of the non-linear absorption changes, which is different than most definitions of the switching intensity. Most definitions in the literature are from all-optical switching applications where the material has already been placed in a tuned cavity [20], but this definition is for a specific HMM in free space. The definition used in this work makes sense for the special behavior of the HMMs as compared to other materials.

The other property optimized for is the switching width, which is defined as the difference in transmission between the lowest transmission state and the highest transmission state. However, there is one issue that can arise with this in practice, since in some cases, higher order effects, such as fifth-order effects, can cause the modeled switching width to be lower than the actual third-order effects predict. To avoid this, the maximum input intensity in the model was capped at the largest intensity used in the measurements, 200 GW/cm^2, since above that intensity fifth-order effects started to appear. This allows for fair comparison between model and measurement, which will be discussed in section 3.3. These two properties are chosen as the outputs, but the inputs that are optimized over are the design geometries.

The design geometries are simply a pair of metal layer and dielectric layer thicknesses, with a random number of periods. Of course, there are bounds on design space that represent fabrication limits. The number of periods is allowed to vary from 6 to 12 and the layer thicknesses are allowed to vary from 40 to 200 nm, as less than 4 periods or 40 nm makes the effective medium properties less accurate, and more than 12 periods or 200 nm leads to long fabrication times. Source [29] found that the Maxwell-Garnett EMA matched their full electromagnetic field simulations for HMM structures with greater than 4 periods, and previous experimental work associated with this project [30] demonstrated that thinner layers lead to more error in the ellipsometry results. This leads to a modeling framework for a genetic optimization algorithm as follows:

1. For a specific number of population members, design geometries are randomly generated. The parameters of the design geometries are listed above, and they are each given a random value between the bounds.*

2. The linear and non-linear properties of each of those geometries are derived using the Maxwell Garnett EMA, the TTM, and the non-linear effective medium, specifically the result of Eqs. (1) and (5).*

3. These properties and geometries are inserted into *Lumerical*, and the electric fields throughout the simulation domain are calculated for a range of intensities.

4. The electric input and output fields, before and after the sample, are used to calculate the intensity dependent transmission, which can be analyzed to evaluate the objective functions of switching intensity and switching width.

5. The population then evolves according to the genetic algorithm, and the process returns to step 2 and repeats until the max number of generations is reached.*

For actual optimization, the full modeling framework takes too long to run for interrogation of the entire design space, so instead of running the full modeling scheme, a partial scheme was used separately to optimize for properties that corresponded to the desired behavior. This partial scheme consists of the starred steps in the above modeling process. This correspondence was

Optical Materials EXPRESS

verified by running the full modeling framework for a limited population size, and observing that optimal points were the same as the partial scheme.

The two properties that were chosen to optimize for, which in this scheme means maximized, are the absolute value of the non-linear absorption coefficient and the absolute value of the derivative of linear transmission with respect to wavelength. Reference [11] found a correlation between the absolute value of the derivative of linear transmission and the switching capabilities of HMMs, and it is clear that a stronger absorption coefficient will correspond a lower intensity where this switching behavior can be observed. The results of this optimization are shown in the next section. The absolute values need to be used for each parameter since these values can theoretically be positive or negative, to avoid how taking the maximum of positive and negative values would lead to ignoring the negatives.

The outputs, or objective functions, were chosen to be the absolute value of the non-linear absorption and the absolute value of the derivative of the linear transmission. The inputs are simply the constituent material properties, the geometry, and the wavelength. Note that this partial scheme can be used for other applications by selecting different optimization variables [31].

3. Results and discussion

3.1. Optimized designs

The actual optimal designs were found using scheme described above implemented into MATLAB as discussed in the previous section. For the genetic algorithm, 200 population members with 1000 maximum generations was used to investigate the entire design space. Since there are two objective functions, the optimal designs make up a 2D Pareto front, which is a curve. Each population member is represented by a dot, and there is a one-to-one correspondence between specific design parameters and results. There are not necessarily 200 points on each Pareto plot, since some points will be the same. Figure 2 shows the results of the optimization.

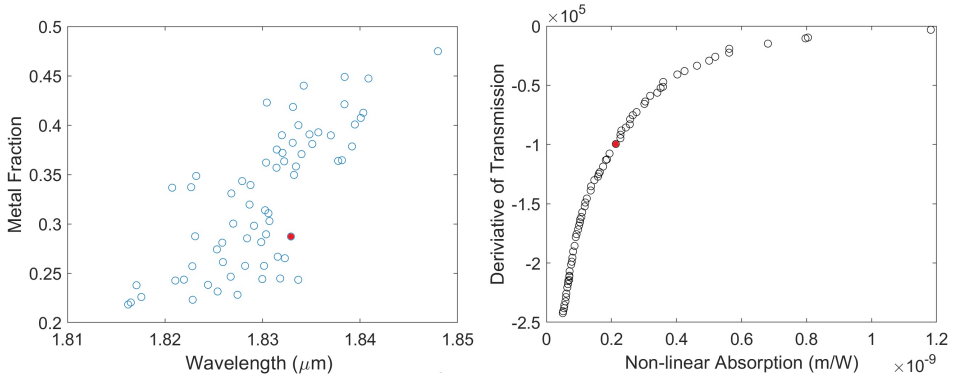

Fig. 2. Pareto front in input parameter space (left plot) and output function space (right plot). For the output plot, the absolute values were used for the optimization, but here the actual values are shown on the axes. The output space plot shows a trade-off that can be made between the derivative of transmission and the maximal non-linear absorption. This corresponds to a trade-off between the switching intensity and switching width. The input plot appears to be more scattered, however, this is simply because the optimal points are grouped closely, so randomness in the genetic algorithm plays a large role. Note that the optimal wavelength for a 29% metal fraction geometry is around 1.835 microns from the parameter space plot, and that 29% metal design corresponds to a derivative of transmission of $-1 * 10^5$ and a non-linear absorption of $0.2 * 10^{-9} m/W$ on the function space plot. The chosen Pareto point for fabrication is highlighted in red on both plots.

Optical Materials EXPRESS

Note any of the points on the input plot could be considered optimal designs, but for this work, the design recipe of a 29% metal fraction was chosen, corresponding to a 55-nm layer of ITO and 135-nm layer of SiO_2. Since all of the Pareto points can be deemed optimal, this was chosen somewhat arbitrarily, after checking on which of the optimal designs would be easiest to fabricate. It is clear that the optimal wavelength is near 1.835 microns for this geometry, but linear measurements showed that the ENZ point of the materials actually falls closer 1.78 to microns, which will be shown from ellipsometry data in the next section. Thus, the optimal point for the special switching will actually occur off of the ENZ point, according to the model.

3.2. Measurements

Ellipsometry was used to get information on the linear properties of the samples. Ellipsometry is a measurement technique that uses polarized light to characterize samples, such as thin films, bulk materials, and layered structures. It measures the relative phase change in polarization states of light reflected off (or transmitted through) the sample's surface. These measurements describe how samples modify the polarization state at each angle of incidence [32]. The system outputs the amplitude (Ψ) and phase (Δ) for each chosen incidence angle over the desired spectral range.

Once experimental data is obtained, then a model of the material is created in accompanying software. In the case of a J.A. Woollam ellipsometer, the software WVASE32 or CompleteEASE [33] is used with the following process. Each layer of a layered material is modeled separately. The software contains a database of materials with bulk optical constants that can be used for each layer. When creating a layer, a material and a layer thickness is chosen. Once a basic model is created, the next step is to fit the model to match the experimental data. This is accomplished by calculating the mean squared error (MSE) between the model's predictions and the experimental data, and then adjusting fit parameters to minimize the MSE.

Using this fit process, it was possible to confirm that the ITO layers did fit well to Drude model, with a MSE of 4.7, and that the M-G EMA did work for modeling the linear properties of the fabricated HMMs, with a MSE of 20.7, which is in the range generally regarded as a successful fit [33,34]. The results for the constituent parameters were as follows: SiO_2 had a refractive index $n = 1.46$, and the Drude model parameters for ITO are $\epsilon_\infty = 3.8005$, $\omega = 3.55 \times 10^{14}$ Hz, and $\gamma = 0.105\omega$.

Once the linear measurements have been completed, the non-linear measurements are covered. To analyze the non-linear properties of the HMMs, the Z-scan technique was used. Z-scan is a well-known technique that illuminates the sample with a focused high power laser beam normal to its surface (the z-direction), and translates the sample through that focus [35–37]. It can be done in transmission or reflection configurations, but this work exclusively used the transmission configuration. Figure 3 shows a diagram of the Z-scan setup.

Z-scan data was taken at 1.78 and 1.835 microns with a peak intensity range of about 20-200 GW/cm^2. For this case, the laser used was a pulsed optical parametric oscillator (OPO) system with a repetition rate of 10 KHz and a pulse width of 150 fs, allowing for the high peak intensity necessary to observe non-linear effects. Amplified Ge detectors were used due to their sensitivity in the wavelength regions of interest. This work is focused on non-linear absorption, so the open aperture configuration of the Z-scan was used.

Note that the measurements were all taken using TM polarization in order to observe the angle-dependent field enhancement, which was obtained by placing a polarizer in the beam path. To get angle dependent data, the sample was placed on a rotating stage, so when referring to the diagram in Fig. 3, the curved arrow shows the direction of rotation. The result of the Z-scan is a detector voltage for each Z-position, and there are different ways to show the data. In this work, normalized transmission is used. The real transmission can be calculated easily with Z-scan using the detector voltage with no sample compared to the detector voltage with a sample, and then this real transmission value can be normalized to the value far away from the focus, where

Optical Materials EXPRESS

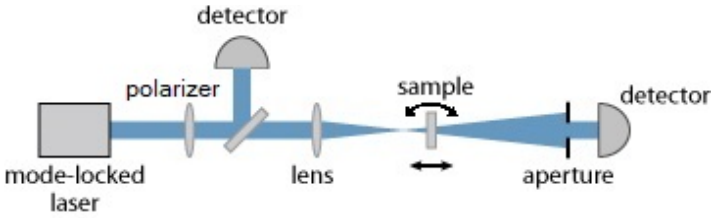

Fig. 3. Diagram of Basic Z-scan Setup. The Z-scan method can be used to calculate the non-linear absorption coefficient and the non-linear refractive index. The detector split off the main beam path is used to monitor power fluctuations in the laser, which allows for more accurate results. If the aperture is closed to the point it cuts off part of the beam, the system is in the closed configuration, otherwise it is in the open configuration.

the incident intensity is much lower and linear effects dominate. This means that any divergence from a transmission of one in the normalized transmission plots shows some non-linear effect. Figure 4 shows the normalized transmission versus the Z-position for the different wavelengths.

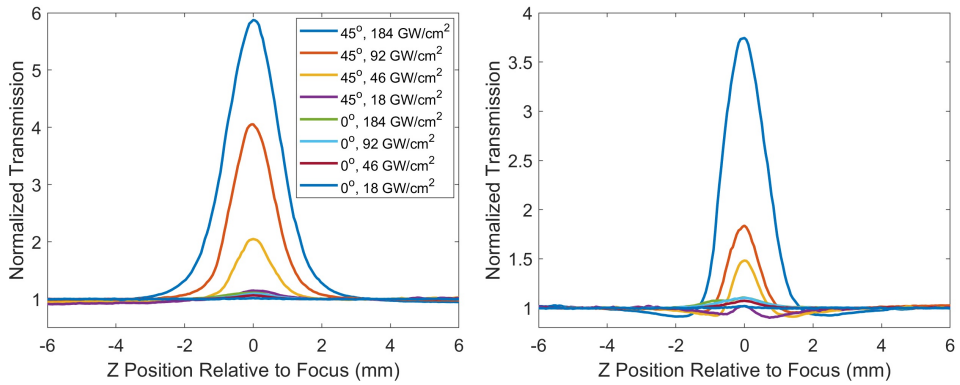

Fig. 4. Open aperture (OA) Z-scan measurements at 1.78 and 1.835 micron wavelengths. The plot on the left is 1.78 microns, while the right is 1.835 microns. Both show the strong field enhancement at an oblique angle for non-linear absorption. The magnitude of the results matches with Ref. [21], which were taken at a similar peak intensity. There is no sign changing behavior in the 1.78 micron data, but there is in the 1.835 micron data, as seen when the normalized transmission becomes less than 1, then becomes greater than 1. In general, the intensity increases as the Z position gets close to the focus, which is set to 0.

The first wavelength investigated was 1.78 μm, near the ENZ point of the HMM. At this wavelength, the largest field enhancement of the material was observed as expected [21], but as stated in section 3.1, this is not the optimal wavelength to observe the actual switching behavior. This data serves as a valuable point of comparison for confirming the model predictions. The next wavelength measured was 1.835 μm, which is the optimal wavelength that came out of the optimization scheme.

Figure 4, in the right-hand plot, shows that at the design wavelength of 1.835 μm, behavior occurs where the sign of the non-linear absorption coefficient changes from positive to negative. To rule out any confounding factors, Z-scan measurements of blank substrates were run, and nothing out of the ordinary was found. Also, multiple samples that were fabricated on different days were all found to have this sign-changing effect. Combined with the strong match of the modeled optimal wavelength to the wavelength where this special behavior is observed, it can be concluded that the cause of this behavior is the special properties of the HMMs.

Optical Materials EXPRESS

The proposed explanation for the behavior is at 45 degrees and lower intensity the properties of the HMM are such that it would naturally exhibit saturable absorption, and for the behavior at higher intensity, the effective properties caused by the increase in electron density create a shift to reverse saturable absorption, which is then strengthened by the field enhancement. This is clearly a property of the HMM, since for isotropic materials, changing the input angle only could change field enhancement, and not the linear properties of the material. The anisotropic nature of HMMs allows for special effective non-linear properties and an increased switching width due to control over the linear optical properties at each angle, remembering that the effective non-linear properties are simply the change from the linear properties.

3.3. Model to measurement comparison

Once the novel behavior was confirmed with measurement, the next step is to confirm that the model is accurately capturing this behavior, accounting for measurement uncertainty. In this section, to calculate the model values for comparison, the full model was used, including FDTD simulations in *Lumerical*, rather than just the MATLAB portion. Figure 5 shows a visual explanation of the switching intensity and switching width.

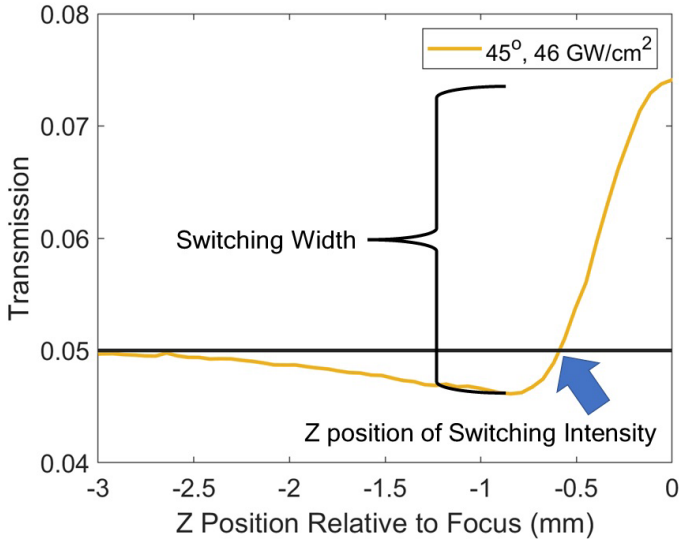

Fig. 5. Visual Explanation of the Switching Width and Intensity. The data in the plot is one of the data sets from Fig. 5, with the black line representing the linear transmission. Note that real transmission is plotted on the y-axis instead of normalized transmission, which is different than Fig. 5. The switching width is simply the difference between the maximum and minimum transmission. The switching intensity is the intensity where the sign of the non-linear absorption coefficient changes from positive to negative. Knowing the z position of the switching intensity to some uncertainty allows for the calculation of the switching intensity.

The measurement uncertainty in the switching width was accounted for by calculating the variance in detector voltage for the Z-scan measurements. This value is small, generally the noise is less than 5%, but this uncertainty acts more as a noise floor, so with very small signals, the relative uncertainty can be higher. Note that this is calculated after removing the power fluctuations from the signal, as discussed in Fig. 4. For all the uncertainty analysis, the partial derivatives of the defining equation are calculated, and are added in quadrature to derive an equation for the standard deviation of the quantity in question. The derivation process itself will

Optical Materials EXPRESS

not be shown, as it is not necessary for understanding of the method. Equation (6) defines the switching width, while Eq. (7) defines the switching width standard deviation.

$$SW = \frac{V_{max}}{V_{air}} - \frac{V_{min}}{V_{air}}, \tag{6}$$

$$\sigma_{SW} = SW\sqrt{2\left(\frac{\sigma_{V_{air}}}{V_{air}}\right)^2 + \left(\frac{\sigma_{V_{max}}}{V_{max}}\right)^2 + \left(\frac{\sigma_{V_{min}}}{V_{min}}\right)^2}, \tag{7}$$

where V_{max} is the maximum detector voltage recorded for the sample, V_{min} is the minimum detector voltage for the sample, V_{air} is the detector voltage with no sample, and SW is the switching width. In this case, $\sigma_{V_{max}}$ and $\sigma_{V_{min}}$ are the same, since they come the from the same measurement.

For the switching intensity, the z position of the switching intensity can be found from the Z scan data. There is uncertainty in this location, since the Z-scan data is only sampled at some discrete Z positions. In this work, 100 points linearly spaced points between the Z positions relative to focus of −6 to 6 were used. For the calculation, the actual intensity is needed, which can be calculated using Gaussian beam propagation. The beam waist of the laser, ω_0, was measured using a knife edge to be 15.2 microns, with an uncertainty of 1 micron, and the Rayleigh length, Z_R, to be 536 microns, also with an uncertainty of 1 micron. Equation (8) shows the formula to calculate the beam radius at any Z position [38], while Eq. (9) shows the uncertainty equation.

$$\omega = \omega_0\sqrt{1 + \frac{z^2}{Z_R^2}}, \tag{8}$$

$$\sigma_\omega = \sqrt{\omega\left[\left(\frac{\sigma_{\omega_0}}{\omega_0}\right)^2 - \left(\frac{\sigma_z \times z}{Z_R^2 \times \omega}\right)^2 + \left(\frac{\sigma_{Z_R} \times z^2}{Z_R^3 \times \omega}\right)^2\right]}, \tag{9}$$

where ω is the beam radius at position z. Next, the average power of the beam was measured using an Ophir power meter, which can be configured to give the standard deviation in its measurements. This average power measurement was performed in the same location as the sample before each Z-scan measurement, since using the same location prevents any errors from losses in the optical train. Using the properties of the laser, namely the repetition rate of 10 kHz and the pulse width of 150 fs, this can be converted into peak power, with an accompanying standard deviation. Note that the repetition rate and pulse width are assumed to have no uncertainty, since their uncertainty should be very small compared to the other factors. Then standard deviation for the power is simply the known standard deviation in the average power divided by the duty cycle, which is $1.5 * 10^{-9}$. Equation (10) shows the calculation of the switching intensity, while Eq. (11) is the calculation of the standard deviation.

$$SI = \frac{P_{peak}}{\pi\omega^2}, \tag{10}$$

$$\sigma_{SI} = \frac{SI}{\pi}\sqrt{\left(\frac{\sigma_{P_{peak}}}{P_{peak}}\right)^2 + \left(\frac{2\sigma_\omega^2}{\omega}\right)^2}, \tag{11}$$

where P_{peak} is the peak power. Figure 6 shows the results of Eqs. (6)–(11).

When considering the results of the comparisons in Fig. 6, it is important to note that while all the measurement uncertainty has been accounted for, there is still the fact of imperfect fabrication, which is not in the models. In the model, perfectly flat layers, as well as consistent layer thickness, are used, therefore the remaining divergence between measurement and the model is attributed to

Optical Materials EXPRESS

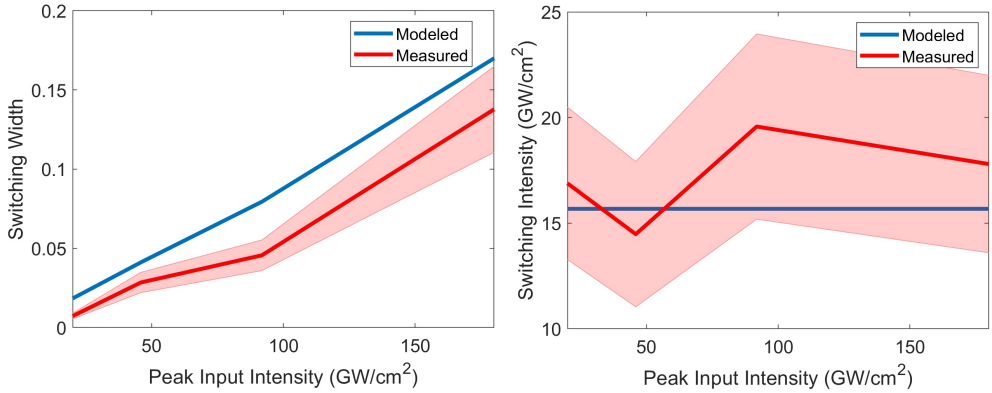

Fig. 6. The measured and modeled properties of the sample, with measurement uncertainties. The left plot shows the switching width, while the right plot shows the switching intensity. The solid line represents the modeled or measured values, while the lighter region represents the uncertainty. There is a systematic bias of the model to produce a larger switching width than the measurement, which is likely due to the fabrication being slightly off from the design as discussed in section 2.1. For the switching intensity, the uncertainty is larger, which is mainly due to the uncertainty in determining the actual z position of the intensity. This could be reduced in the future by using a finer sampling in the Z-scan measurement. Theoretically, the switching intensity should not change with input intensity, which is represented in the modeled values. Note that the model is within the bounds of the measurement uncertainty.

fabrication challenges. However, the general behavior and trends in the HMMs are represented well. In the future, even better fabrication of these layered samples could lead to more accurate models.

The switching width and switching intensity measured and modeled in this work are similar to the few other results for non-linear HMMs. Source [11] used simulation to design HMMs for optical switching, and calculated switching widths ranging from 0.05 to 0.15, with switching intensities near 1 GW/cm^2. The current work requires a larger intensity, which is likely due to the fact that source [11] used a different material system with gold or silver as the metal layer and an operating wavelength in the visible. For a layered ITO/SiO_2 HMM, Source [14] quotes a switching width defined as −5.17 dB for an input intensity of about 140 GW/cm^2 after converting from pulse fluence values. Converted into dB, the maximum switching width observed in this work is −6.2 dB at an input intensity of 180 GW/cm^2. So this work has demonstrated similar performance to source [14], which used the exact same material system ITO/SiO_2, and similar modeling techniques. This gives confidence that the modeling results presented in this work are reasonable, and the measurement results which are unique to this work support the modeling conclusions of both groups.

4. Conclusion

Novel behavior involving switching of the non-linear absorption in an ITO/SiO_2 hyperbolic metamaterial has been modeled, optimized for, and experimentally verified. The fabrication method and modeling methods were discussed, and then the results were presented. This showed a large enhancement of the effective non-linear properties, in which switching behavior where the sign of the non-linear absorption coefficient changes from positive to negative. This switching behavior has a switching intensity near 15 GW/cm^2 and switching width of about 0.15.

The applications of this behavior include advanced optical switches or optical limiters as well as other applications such as cavity materials for high power laser sources, since having

Optical Materials EXPRESS

more control over the transmission state and even having more transmission states available would be useful in all those applications. In general, the switching time of devices built on HMMs will be fast, which increases potential for applications. Previous research has found switching times in the hundreds of femtoseconds for HMM-based switches [11]. More research is recommended to investigate related areas, where different properties could be chosen to optimize for in either a full field computational scheme or a closed fast running scheme. Choosing different objective functions could allow for quick optimization of many other devices. Some examples of other properties to test for include enhancement of non-linear refraction in a material with low linear absorption and non-linear absorption, optimization of second harmonic generation in non-centrosymmetric materials, and optimization of spontaneous parametric down-conversion for single photon applications.

One area of future work would be to test the same concept with other material systems. It is possible that much stronger switching behavior could be achieved with a different material system, such as switching out the plasmonic material for gold or titanium nitride. Another avenue is to consider active modulation of the properties of the ITO layer, possibly by applying a voltage [39]. This could provide even more tunability of the non-linear properties.

Funding. Air Force Office of Scientific Research (2018-109, 2021-094).

Acknowledgments. J. Ethridge thanks AFOSR/RTB1 for funding this research. J. Ethridge thanks Cynthia Bowers for assistance with TEM imagery of samples, and Carl Liebig for assistance with Z-scan measurements.

Disclosures. The authors declare no conflicts of interest.

Data availability. Data underlying the results presented in this paper are not publicly available at this time but may be obtained from the authors upon reasonable request.

References

1. P. Shekhar, J. Atkinson, and Z. Jacob, "Hyperbolic metamaterials: fundamentals and applications," Nano Convergence **1**(1), 14 (2014).
2. A. Poddubny, I. Iorsh, P. Belov, and Y. Kivshar, "Hyperbolic metamaterials," Nat. Photonics **7**(12), 948–957 (2013).
3. L. Ferrari, C. Wu, D. Lepage, X. Zhang, and Z. Liu, "Hyperbolic metamaterials and their applications," Prog. Quantum Electron. **40**, 1–40 (2015).
4. E. G. Mironov, L. Liu, H. T. Hattori, and M. Richard, "Analysis of silica-filled slot waveguides based on hyperbolic metamaterials," J. Opt. Soc. Am. B **31**(8), 1822–1828 (2014).
5. Y. Guo, C. L. Cortes, S. Molesky, and Z. Jacob, "Broadband super-planckian thermal emission from hyperbolic metamaterials," Appl. Phys. Lett. **101**(13), 131106 (2012).
6. Y. Guo and Z. Jacob, "Thermal hyperbolic metamaterials," Opt. Express **21**(12), 15014–15019 (2013).
7. A. N. Poddubny, I. V. Iorsh, and A. A. Sukhorukov, "Generation of photon-plasmon quantum states in nonlinear hyperbolic metamaterials," Phys. Rev. Lett. **117**(12), 123901 (2016).
8. C. Cortes, W. Newman, S. Molesky, and Z. Jacob, "Quantum nanophotonics using hyperbolic metamaterials," J. Opt. **14**(6), 063001 (2012).
9. S. Kim, J. Jin, Y.-J. Kim, I.-Y. Park, Y. Kim, and S.-W. Kim, "High-harmonic generation by resonant plasmon field enhancement," Nature **453**(7196), 757–760 (2008).
10. M. Shoaei, M. K. Moravvej-Farshi, and L. Yousefi, "All-optical switching of nonlinear hyperbolic metamaterials in visible and near-infrared regions," J. Opt. Soc. Am. B **32**(11), 2358–2365 (2015).
11. M. Kim, S. Kim, and S. Kim, "Optical bistability based on hyperbolic metamaterials," Opt. Express **26**(9), 11620–11632 (2018).
12. A. D. Neira, G. A. Wurtz, P. Ginzburg, and A. V. Zayats, "Ultrafast all-optical modulation with hyperbolic metamaterial integrated in si photonic circuitry," Opt. Express **22**(9), 10987–10994 (2014).
13. E. Azmoudeh and S. Farazi, "Ultrafast and low power all-optical switching in the mid-infrared region based on nonlinear highly doped semiconductor hyperbolic metamaterials," Opt. Express **29**(9), 13504–13517 (2021).
14. Z. T. Xie, Y. Sha, J. Wu, H. Y. Fu, and Q. Li, "Ultrafast dynamic switching of optical response based on nonlinear hyperbolic metamaterial platform," Opt. Express **30**(12), 21634–21648 (2022).
15. T. Tumkur, G. Zhu, P. Black, Y. A. Barnakov, C. Bonner, and M. Noginov, "Control of spontaneous emission in a volume of functionalized hyperbolic metamaterial," Appl. Phys. Lett. **99**(15), 151115 (2011).
16. J. Kim, V. P. Drachev, Z. Jacob, G. V. Naik, A. Boltasseva, E. E. Narimanov, and V. M. Shalaev, "Improving the radiative decay rate for dye molecules with hyperbolic metamaterials," Opt. Express **20**(7), 8100–8116 (2012).
17. M. Hajizadegan, M. Sakhdari, and V. Ahmadi, "Design of a Kerr effect based terahertz all-optical switch using metallic nanocomposite metamaterial structure," in *2012 Second Conference on Millimeter-Wave and Terahertz Technologies (MMWaTT)*, (IEEE, 2012), pp. 5–8.

Optical Materials EXPRESS

18. R. W. Boyd, *Nonlinear Optics* (Academic Press, 2019).
19. W. Chen, K. M. Beck, R. Bücker, M. Gullans, M. D. Lukin, H. Tanji-Suzuki, and V. Vuletić, "All-optical switch and transistor gated by one stored photon," Science **341**(6147), 768–770 (2013).
20. T. Tanabe, M. Notomi, S. Mitsugi, A. Shinya, and E. Kuramochi, "Fast bistable all-optical switch and memory on a silicon photonic crystal on-chip," Opt. Lett. **30**(19), 2575–2577 (2005).
21. M. Z. Alam, I. De Leon, and R. W. Boyd, "Large optical nonlinearity of indium tin oxide in its epsilon-near-zero region," Science **352**(6287), 795–797 (2016).
22. L. Sun, J. T. Grant, J. G. Jones, and N. R. Murphy, "Tailoring electrical and optical properties of al-doped zno thin films grown at room temperature by reactive magnetron co-sputtering: from band gap to near infrared," Opt. Mater. **84**, 146–157 (2018).
23. N. R. Murphy, R. C. Gallagher, L. Sun, J. G. Jones, and J. T. Grant, "Optical and chemical properties of mixed-valent rhenium oxide films synthesized by reactive dc magnetron sputtering," Opt. Mater. **45**, 191–196 (2015).
24. M. Born and E. Wolf, *Principles of Optics: Electromagnetic Theory of Propagation, Interference and Diffraction of Light* (Elsevier, 2013).
25. N. Rotenberg, A. Bristow, M. Pfeiffer, M. Betz, and H. Van Driel, "Nonlinear absorption in Au films: role of thermal effects," Phys. Rev. B **75**(15), 155426 (2007).
26. R. W. Boyd, R. J. Gehr, G. L. Fischer, and J. Sipe, "Nonlinear optical properties of nanocomposite materials," Pure Appl. Opt. **5**(5), 505–512 (1996).
27. P. Kabaciński, T. M. Kardaś, Y. Stepanenko, and C. Radzewicz, "Nonlinear refractive index measurement by SPM-induced phase regression," Opt. Express **27**(8), 11018–11028 (2019).
28. D. Whitley, "A genetic algorithm tutorial," Stat. Comput. **4**(2), 65–85 (1994).
29. J. Sukham, O. Takayama, M. Mahmoodi, S. Sychev, A. Bogdanov, S. H. Tavassoli, A. V. Lavrinenko, and R. Malureanu, "Investigation of effective media applicability for ultrathin multilayer structures," Nanoscale **11**(26), 12582–12588 (2019).
30. J. A. Ethridge, J. G. Jones, M. R. Ferdinandus, M. J. Havrilla, and M. A. Marciniak, "Linear and nonlinear properties of ITO/SiO_2 layered metamaterials," Proc. SPIE **11796**, 117960U (2021).
31. J. A. Ethridge, J. G. Jones, M. D. Ferdinandus, M. J. Havrilla, and M. A. Marciniak, "Efficient optimization of nonlinear optical devices with ITO/SiO_2 layered hyperbolic metamaterials," Proc. SPIE **11997**, 37–45 (2022).
32. H. Tompkins and E. A. Irene, *Handbook of Ellipsometry* (William Andrew, 2005).
33. J. A. Wollam, *Guide to Using WVASE Spectroscopic Ellipsometry Data Acquisition and Analysis Software* (J. A. Wollam Co. Inc, 1994).
34. J. Pflüger and J. Fink, *Handbook of Optical Constants in Solids II* (Elsevier, 1991).
35. W. Zhao and P. Palffy-Muhoray, "Z-scan technique using top-hat beams," in OSA Annual Meeting (Optica Publishing Group, 1993), pp. MHH–1.
36. P. Chapple, J. Staromlynska, J. Hermann, T. Mckay, and R. McDuff, "Single-beam z-scan: measurement techniques and analysis," J. Nonlinear Opt. Phys. Mater. **06**(03), 251–293 (1997).
37. E. W. Van Stryland and M. Sheik-Bahae, "Z-scan measurements of optical nonlinearities," Characterization techniques and tabulations for organic nonlinear materials **18**, 655–692 (1998).
38. W. Koechner, *Solid-state Laser Engineering*, vol. 1 (Springer, 2013).
39. S. Stankowski and J. J. Ramsden, "Voltage-dependent coupling of light into ito-covered waveguides," J. Phys. D: Appl. Phys. **35**(4), 299–302 (2002).